S & M 4584

Spatiotemporal Thermal Fault Prediction for Electromechanical Equipment Using High-density Sensor Arrays and Attention-enhanced Algorithm

Xuemei Yu,[1*] Feifei Xing,[1] Bingtao Liu,[2] Nan Zhang,[2] and Jie Zhu[2]

[1]Beijing Polytechnic University, No. 9, Liangshuihe 1st Street,
Beijing Economic and Technological Development Area, Beijing, China
[2]China Construction Fourth Engineering Bureau Co., Ltd., Beijing Branch,
Huiya Building, Lize Business District, Fengtai District, Beijing, China

(Received May 11, 2026; accepted August 4, 2026)

Keywords: thermal fault prediction, temperature sensor array, building electromechanical equipment, mathematical model

The stable operation of electromechanical equipment is vital for modern infrastructure. However, thermal faults remain a leading cause of unexpected shutdowns. Traditional single-point monitoring and infrared (IR) inspections often fail to detect incipient, localized anomalies owing to limited timeliness and spatial resolution. Therefore, we developed a predictive system based on high-density temperature sensor arrays and advanced spatiotemporal modeling. In the system, an optimized 64-channel Class A PT100 resistance temperature detector topology with MAX31865 converters was deployed to capture dynamic thermal fields. A complete preprocessing pipeline, including denoising and feature engineering, ensured data integrity by suppressing stochastic hardware noise. The prediction model was established by integrating convolutional long short-term memory (ConvLSTM) with a convolutional block attention module (CBAM), focusing on critical spatial regions. Quantile regression analysis was used for probabilistic fault estimation and a multi-level warning system. The validation results of the system performance on a 75 kW pump for three months demonstrated that the ConvLSTM + CBAM model showed a mean absolute error of 0.50 °C, a 23% improvement over the ConvLSTM model. The model extended the average fault warning lead time to 52 min, representing a 150% increase compared with that of the LSTM model. These results show that dense sensor arrays combined with attention-based deep learning deliver accurate thermal diagnostics comparable to IR imaging, offering a scalable solution for proactive industrial maintenance.

1. Introduction

With the advancement of modern architecture with intelligent, high-density configurations,[(1)] the scale and complexity of integrated mechanical and electrical (M&E) systems have become

*Corresponding author: e-mail: 101519@bpu.edu.cn
https://doi.org/10.18494/SAM6413

ISSN 0914-4935

significant.[2] These systems prolong high-load operation by effectively preventing and managing mechanical wear and electrical contact degradation, being more susceptible to various malfunctions than without the systems. Thermal faults of electromechanical equipment caused by abnormal exothermic behavior account for a significant proportion of equipment failures.[3,4] Localized increases in contact resistance or insufficient bearing lubrication can generate anomalous temperature gradients, which lead to thermal faults. If they are not timely detected, thermal faults might cause equipment breakdowns, electrical fires, or systemic paralysis, with severe economic and safety consequences.[5]

Current electromechanical equipment monitoring methods rely largely on periodic manual inspections,[6] handheld infrared (IR) thermography,[7] and threshold-based alarms from discrete single-point temperature sensors.[8] However, manual inspections are subjective and lack the immediate resolution for continuous monitoring. Although IR thermography enables the high-resolution spatial mapping of surface temperatures, the application of this method is constrained by high costs and environmental sensitivity, limiting its use to fault diagnostics.[9] Various sensors are also used for the continuous monitoring of electromechanical equipment. However, utilizing the sensor data might suffer from placement bias, since their positioning in current methods is guided by empirical heuristics that overlook stochastic hotspots and fail to capture the complex spatiotemporal dynamics of equipment thermal fields.[10]

Recently, advances in IoT and flexible electronics have enabled the widespread deployment of high-density, cost-effective temperature sensor arrays on complex surfaces in electromechanical equipment.[11,12] These sensor arrays enable the generation of pixelated thermal data, capturing the temporal evolution of individual nodes and the spatial correlations within the sensor network. Such fine-grained sensing methods are used to characterize device thermal states and detect incipient anomalies.[13] However, the high dimensionality of the sensor datasets necessitates advanced analytical algorithms. Deep learning models, particularly recurrent neural networks (RNNs) and long short-term memory (LSTM) models, have shown exceptional capability in processing nonlinear time-series data.

Therefore, in this study, we integrate distributed sensors with predictive spatiotemporal algorithms to transform fault detection for proactive thermal trend forecasting to enhance the reliability and resilience of the sensor-based diagnosis of the electromechanical equipment.[14]

2. Temperature Sensor Array Architecture

2.1 Thermal characteristics of M&E equipment

To optimize the deployment of sensor arrays, the heat generation mechanisms and thermal distribution profiles of the monitored object must be characterized.[15,16] We employed a large centrifugal water pump unit as the basis for designing the sensor array and developing the corresponding matching algorithms, since the water pump unit is a critical component in heating, ventilation, and air conditioning systems. The thermal sources in the water pump unit are identified as follows.

- Motor section: Thermal energy is generated through copper losses in the stator windings, iron losses in the core, and wind friction. Under nominal conditions, heat is concentrated within the internal windings and dissipated through the casing and cooling fins. Incipient faults, such as inter-turn short circuits or mechanical overloads, manifest as localized, high-gradient temperature spikes.[17]
- Pump and bearing casings: Thermal anomalies originate from fluid friction and mechanical friction within rolling or sliding bearings. Failures in lubrication, progressive component wear, or shaft misalignment typically result in abnormal heat accumulation at the bearing housings.
- Couplings and seals: Torque transmission and mechanical sealing generate frictional heat. Misalignment at the coupling interface or the degradation of the shaft seals creates localized hotspots, which serve as indicators of mechanical failure.

Figure 1 presents the IR thermal image of the water pump unit, highlighting important regions of temperature increase under normal operating conditions. These regions, along with their adjacent areas, represent the most probable sites of thermal faults and therefore constitute the primary focus for sensor deployment.

2.2 Sensor layout optimization

The sensor array was designed to enhance the signal integrity and the sensitivity of the diagnosis of the electromechanical equipment (Fig. 2).[18,19] We adopted a nonuniform hybrid topology governed by the following principles. Figure 2 shows the optimized distribution of temperature sensors on a simplified computer-aided design of the pump unit, including the motor, coupling, and pump casing. Red dots denote the key areas of dense sensor placement, characterized by high thermal gradients and mechanical stress, whereas blue dots indicate the

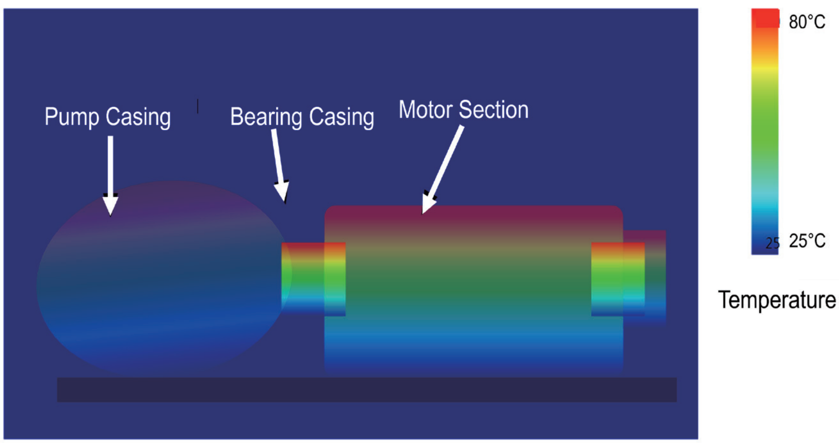

Fig. 1. (Color online) Infrared thermal image of the water pump unit under normal operating conditions (captured in this study).

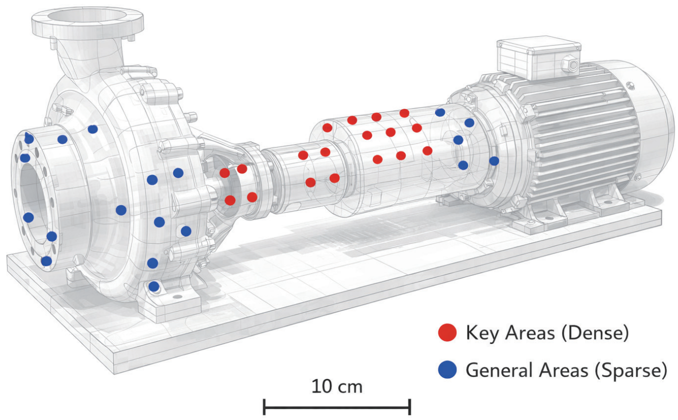

Fig. 2. (Color online) Surface sensor array for water pump unit.

general areas of sparse coverage for baseline monitoring. This sensor layout supports the high-fidelity thermal mapping and early detection of incipient faults such as bearing wear, misalignment, and winding overheating, improving the reliability of thermal diagnostics in rotating machinery.

- High-density hotspot coverage: intensive sensor clustering at primary thermal sources, including the motor section and bearing case
- Gradient-zone mapping: transitional sensor placement between critical and noncritical thermal areas to capture heat flux dynamics
- Sparse monitoring: baseline sensing across uniform-temperature surfaces to detect stochastic anomalies

We modeled the equipment surface in a discretized $M \times N$ grid. To optimize node placement, finite element analysis (FEA) was performed to simulate steady-state heat conduction under various fault scenarios, such as bearing seizure. A genetic algorithm was employed to maximize the fault detection coverage but minimize the total node count. The performance metrics of this optimized layout are summarized in Table 1.

The optimized sensor layout achieved substantial improvements over the initial empirical design while maintaining the same total number of sensors ($n = 64$). The coverage rate of critical thermal-source regions increased from 85 to 98%, demonstrating that the genetic algorithm effectively eliminated thermal blind spots in high-risk areas such as motor windings and bearing seats. Fault-detection sensitivity also improved markedly, increasing from 0.72 to 0.91 (before and after optimization, respectively), which corresponds to a 26.4% gain. This enhancement indicates that the optimized array captured early-stage thermal gradients that might be overlooked in a non-optimized configuration. Layout redundancy was reduced from 15 to 8% by redistributing sensors from low-risk zones to high-gradient regions, thereby achieving a more

Table 1
Performance metrics before and after sensor layout optimization.

Metric	Initial empirical layout	Optimized layout	Performance improvement
Total number of sensors	64	64	—
Coverage rate of critical areas	85%	98%	+13%
Average fault detection sensitivity (simulation)	0.72	0.91	+26.4%
Layout redundancy	15%	8%	−7%

efficient pixelation of the thermal field. The results highlight that intelligent sensor placement is critical, ensuring that the array provides a high-fidelity digital representation of the equipment's thermal state. This optimization directly strengthens the reliability of subsequent deep-learning-based fault prediction models in industrial IoT applications.

2.3 Multi-channel sensor data acquisition

To capture the spatiotemporal dynamics of the thermal field without phase-lag errors, we developed a synchronous acquisition architecture comprising a cascaded bus structure including the following layers (Fig. 3). The arrows and connection lines in the hardware architecture of Fig. 3 represent the control and data transmission workflows of the acquisition system. The red dashed downward arrows indicate the propagation direction of the physical hardware synchronization signal (falling-edge trigger pulse) initiated by the master aggregation unit to force simultaneous conversions across all slave units. The black solid downward arrows at the bottom denote local polling routes where the acquisition slaves query raw sensor data from their assigned sensor subgroups. The remaining solid lines represent bi-directional serial buses through which aggregated thermal vectors are transmitted upward for database archiving and control instructions are sent back down to the edge nodes.

- Sensing layer and multiplexing signal path: The direct connection of 64 independent Class A PT100 Platinum resistance temperature detectors (RTDs) to 64 individual digitizers is economically and physically impractical owing to the massive wiring footprint and high pin-count requirements. To resolve this, we implemented an analog-multiplexed matrix routing architecture. The 64 PT100 sensors were organized into four symmetric clusters of 16 sensors. Each cluster was routed to a low-resistance, low-injection-noise 16-channel analog multiplexer such as ADG726 (Analog Devices, the United States of America), which sequentially switched the differential RTD lines to a single MAX31865 RTD-to-digital converter.[20] This layout reduced the required converter count from 64 to 4.
- Signal conditioning and digitization: The MAX31865 RTD-to-digital converter was used to handle the two-wire RTD configuration and convert the analog resistance values into a 15-bit digital representation using an internal delta-sigma analog-to-digital converter (ADC). To minimize the effects of contact and wire resistance over the multiplexer channels, high-precision reference resistors (R_{REF} = 430 Ω, 0.1% tolerance) were utilized as calibration

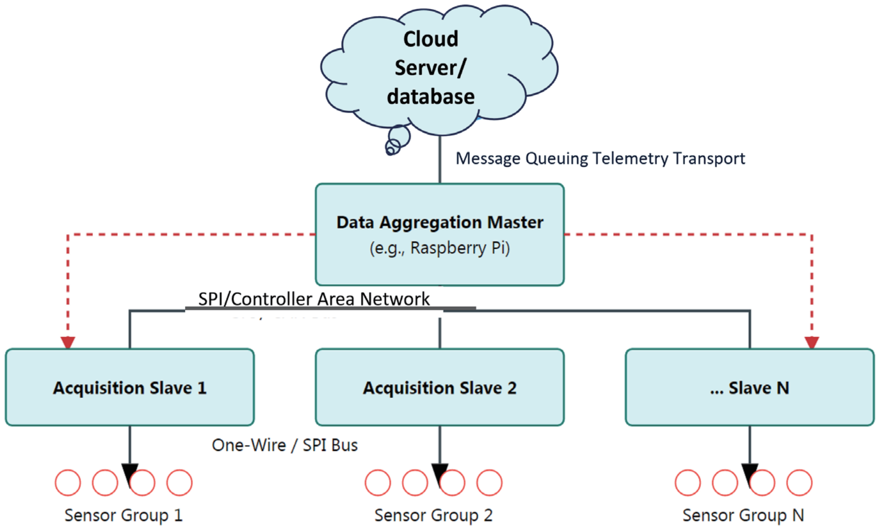

Fig. 3. (Color online) Hardware architecture of multi-channel sensor data acquisition system (arrows and lines denote directional flow of hardware synchronization triggers, local sensor polling, and bi-directional network communication).

targets. The microcontrollers cycled through the multiplexer select lines, allowing a 10 ms settling time per channel before triggering a conversion. The total sweep time for all 64 channels was completed in less than 180 ms, which easily accommodates the 1 Hz sampling frequency required for sluggish thermal diffusion processes. The digitized values were then transmitted from the acquisition slaves to the master aggregation unit via a high-noise-immunity controller area network bus.

- Acquisition slaves: Multiple microcontrollers were used to manage localized sensor subgroups through one-wire or serial peripheral interface protocols of analog devices.
- Hardware synchronization: A master aggregation unit was adopted to trigger a global falling-edge pulse using a dedicated general-purpose input/output pin to all slave interrupt pins. This architecture ensures that the start conversion command is executed across all 64 channels with a synchronization error of shorter than 10 μs.[21] The level of temporal precision is vital for the subsequent deep learning models to correlate spatial heat diffusion accurately.

Table 2 shows the performance parameters of the multi-channel sensor data acquisition system developed in this study.

To ensure that the collected data from the optimized sensor array were reliably and instantly transmitted to the backend server, we adopted the lightweight message queuing telemetry transport protocol.[22,23] In each sampling period, the host aggregates data from all 64 sensors along with high-precision timestamps into a JavaScript Object Notation-formatted string. To reduce transmission load, sensor identifications were encoded as integer indices, and temperature values were scaled by a factor of 100 and rounded to the nearest integer. A hierarchical structure, including build-A-floor-3/havac/pump-01/temperature_array, was

Table 2
Performance parameters of multi-channel sensor data acquisition system.

Parameter	Value	Description
Sensor transduction	PT100 (Class A) + MAX31865	High precision and high stability
Measurement range	−50 to 200 °C	Operating temperature ranges of electromechanical equipment
Measurement accuracy	±0.15 °C	For early fault diagnosis
Resolution	0.03125 °C	15-bit ADC
Synchronization latency	< 10 µs	Guaranteed by hardware synchronization signal
Sampling frequency	1 Hz	Adjustable, 1 Hz suffices for thermal process

implemented to facilitate backend subscription and management. For service quality, the quality of service level was set to 1 (at least one delivery), ensuring successful transmission despite potential network fluctuations. In the event of disconnection, data were temporarily buffered and automatically resent once connectivity was restored. A watchdog timer on the host side safeguarded reliability by triggering local alarms or restarting the network module if multiple consecutive transmission failures occur.

Optimized sensor placement, coupled with robust data transmission protocols, is as critical as hardware accuracy. For industrial IoT applications, this integration forms the basis of a thermal digital twin, which is a high-fidelity, real-time virtual representation that continuously mirrors the spatial heat generation and diffusion across the physical equipment. By coupling low-latency sensor arrays with deep learning forecasting, the digital twin allows operators to simulate, visualize, and predict dynamic thermal fields, thereby transforming point-based anomaly detection into proactive lifecycle diagnostics.[24]

2.4 Data preprocessing and feature engineering

Raw sensor data are often contaminated by electromagnetic interference, producing high-frequency noise or spikes. To address this, we applied the discrete wavelet transform for the time and frequency localization of nonstationary temperature signals. Multi-level wavelet decomposition was also performed, followed by the thresholding of high-frequency coefficients, and reconstruction yields denoised sequences. Missing values due to sensor or communication faults were compensated using a hybrid time–space interpolation.

$$\hat{T}(p,t) = \alpha \cdot \frac{1}{2K} \sum_{k=1}^{K} \big(T(p,t-k) + T(p,t+k) \big) + (1-\alpha) \cdot \frac{\sum_{q \in N(p)} w_{pq} T(q,t)}{\sum_{q \in N(p)} w_{pq}} \tag{1}$$

Here, $\hat{T}(p,t)$ denotes the estimated temperature at sensor p at time t, $T(p,t)$ represents the actual measured value at that sensor and time, K defines the temporal window, specifying how many past and future samples are averaged, and k is the discrete index within that window. The factor

α is used to balance the contribution of temporal smoothing against spatial averaging, $N(p)$ refers to the set of neighboring sensors around sensor p, and w_{pq} is the distance-based weight assigned to neighbor q, with closer sensors contributing more strongly to the estimate. Together, these terms combine temporal information from the same sensor with spatial information from nearby sensors, producing a robust temperature estimate that resists gaps in time series data and inconsistencies across the sensor network.

We calculated Pearson correlation coefficients between sensor pairs to quantify spatial dependence. Figure 4 shows the correlation heatmap. Sensors near bearings (S12–S14) exhibited strong positive correlation, consistent with localized thermal coupling. Individual sensor sequences showed long tails, confirming strong temporal dependence.

Temperature is changed by multiple overlapping factors: periodic cycles from the environment and operating schedule, long-term trends from wear and degradation, and random or fault-related disturbances. By using seasonal–trend decomposition via loess (STL), each sensor's temperature sequence (T) is decomposed into trend, seasonal, and remainder components.

$$T(t) = Trend(t) + Seasonal(t) + Remainder(t) \tag{2}$$

The remainder component isolates abnormal fluctuations, offering an input feature for fault detection. Because the sensor array produced high-dimensional data (64 channels), direct input into a model risks overfitting. To reduce dimensionality, principal component analysis was conducted by projecting the data onto orthogonal bases that maximize variance. Each time step was treated as a 64-dimensional vector, and PCA was performed across the dataset. Variables including temperature, humidity, and equipment load were normalized using the minimum-maximum scaling method. The variables were used as inputs to the model along with temperature characteristics. Table 3 shows the cumulative variance contribution rate of the

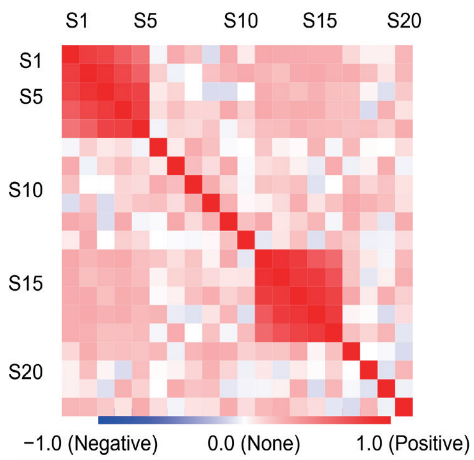

Fig. 4. (Color online) Heatmap of sensor temperature sequence correlation.

Table 3
Cumulative variance of principal components.

Number of principal components included	Cumulative explained variance (%)
1	68.2
3	85.1
5	92.5
8	97.3
10	98.9
16	99.8

principal components. The first eight components explained 97.3% of the total variance, indicating that the original 64-dimensional vector can be replaced with an 8-dimensional representation without significant information loss.

3. Thermal Fault Prediction Model

A predictive model was established to forecast temperature sequences $X_{t+1},\ldots, X_{t+H}$ for H subsequent time steps, given a historical observation window of $X_{t-(L+1)},\ldots, X_t$ of length L. Here, X_t represents a discretized 2D snapshot of the temperature field acquired from the sensor array at time t. Although traditional long short-term memory (LSTM) models are proficient at time-series analysis, they require the conversion of 2D sensor data into 1D vectors, which removes the inherent spatial correlations of the thermal field. To preserve the inherent spatial correlations that are critical spatial features, we utilized a convolutional LSTM (ConvLSTM) architecture. By replacing the standard affine transformations with convolution operations, ConvLSTM captures the coupled spatiotemporal dynamics of heat diffusion. The state transitions are governed by the following equations:

$$\text{Input gate: } i_t = \sigma\left(W_{xi} * X_t + W_{hi} * H_{t-1} + W_{ci} \circ C_{t-1} + b_i\right), \tag{3}$$

$$\text{Forget gate: } f_t = \sigma\left(W_{xf} * X_t + W_{hf} * H_{t-1} + W_{cf} \circ C_{t-1} + b_f\right), \tag{4}$$

$$\text{Cell state update: } C_t = f_t \circ C_{t-1} + i_t \circ \tanh\left(W_{xc} * X_t + W_{hc} * H_{t-1} + b_c\right), \tag{5}$$

$$\text{Output gate: } o_t = \sigma\left(W_{xo} * X_t + W_{ho} * H_{t-1} + W_{co} \circ C_t + b_o\right), \tag{6}$$

$$\text{Hidden state: } H_t = o_t \circ \tanh\left(C_t\right). \tag{7}$$

Here, X_t is the input vector at time t, $H_{t\text{-}1}$ is the hidden state from the previous time step, $C_{t\text{-}1}$ is the cell state from the previous time step, C_t is the updated cell state, H_t is the updated hidden state, W_x, W_h, are W_x are the weight matrices for input, hidden, and cell connections, respectively, b is the bias term, σ is the Sigmoid activation function, and tanh is the hyperbolic tangent activation function. In the equations, * represents the convolution operation and ∘ represents the Hadamard product. X_t is the input and H_t is the hidden state. i_t, f_t, and o_t are the input, forget, and output gates, respectively. W and b are the weights and biases to be learned, respectively.

The model adopted an encoder-decoder configuration (Fig. 5). The encoder consists of three stacked ConvLSTM layers that ingest the historical L-frame sequence and compress it into a high-dimensional state vector. The decoder, also comprising three layers, uses this vector as an initial state to iteratively generate the predicted thermal frames for the H-step horizon.

In thermal diagnostics, faults are localized for a specific bearing or winding before propagating. Standard ConvLSTM layers process all spatial pixels with uniform weight to dilute the signal of incipient hotspots. To prioritize the critical regions, we integrated a convolutional block attention module (CBAM) to refine feature maps through channel and spatial attention mechanisms.[25] A channel attention module identified the most relevant feature, including a specific thermal gradient. The hidden state underwent global average and maximum pooling to aggregate spatial information into two descriptor vectors. These are processed by a shared multi-layer perceptron to generate the channel weight M_c.

$$M_c(F) = \sigma\left(MLP\left(AvgPool(F)\right) + MLP\left(MaxPool(F)\right)\right) \tag{8}$$

A spatial attention module learned the importance of different spatial positions by taking channel attention-weighted feature maps as input, performing average and maximum pooling on the channel dimension to obtain two feature maps, and then concatenating these two feature maps. Through a convolutional layer and a Sigmoid function, an inter-attention weight M_s was generated. This weight was multiplied by the feature map to highlight important spatial regions.

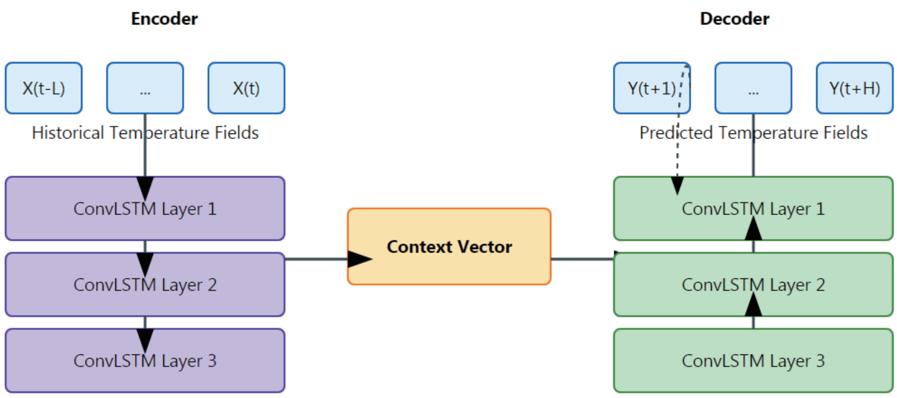

Fig. 5. (Color online) Encoder-decoder prediction model architecture adopting ConvLSTM.

$$M_s(F') = \sigma\left(f^{7\times7}\left(\left[AvgPool(F');MaxPool(F')\right]\right)\right) \tag{9}$$

We embedded CBAM within the encoder layers (Fig. 6) to focus on regions exhibiting abnormal thermal signatures during the encoding of historical data. The model used in this study conducted a single-point estimate (expected value). Figure 6 shows the integration of channel and spatial attention modules within the ConvLSTM encoder to enhance thermal feature localization. The channel attention branch applies global average pooling (AvgPool) and global max pooling (MaxPool) across spatial dimensions, followed by fully connected layers to generate channel weights M_c. The spatial attention branch performs average and maximum pooling across channels, concatenates the resulting maps, and applies a 3 × 3 convolution (3 × 3 Conv) to produce spatial weights M_s.

To estimate predictive uncertainty, quantile regression was conducted to estimate the conditional probability density of future temperatures. Rather than predicting only the median value, the model was trained to output multiple quantiles of 5, 25, 50, 75, and 95%. For a given quantile q, the pinball loss function was defined as

$$Lq\left(y, y^q\right) = \max\left[q\cdot\left(y - y^q\right), (1-q)\cdot\left(y^q - y\right)\right]. \tag{10}$$

Here, y is the true observed value, y^q is the predicted quantile value at the quantile level, q is the quantile level (between 0 and 1, 0.5 for median), and max[·] is used to ensure that the loss penalizes deviations depending on whether the prediction underestimates or overestimates the true value.

By predicting a range of quantiles, we construct confidence intervals for each sensor node. For instance, the [5%, 95%] interval represents a 90% confidence level regarding the equipment's future state. This allows for proactive risk management: if the 95th percentile exceeds a safety threshold, a warning can be issued even if the 50th percentile remains within nominal limits. The proposed fault warning hierarchy is summarized in Table 4.

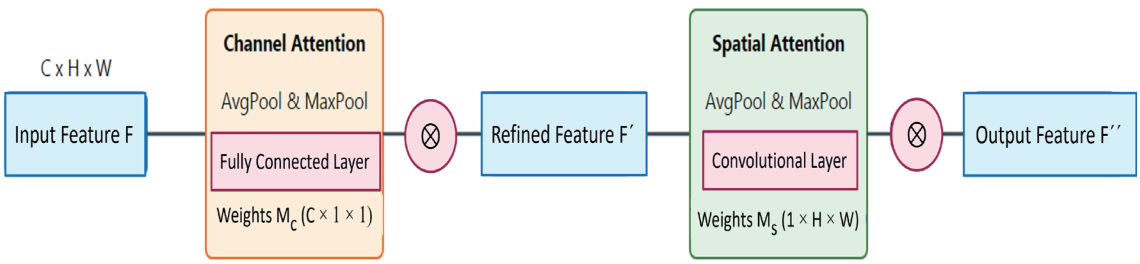

Fig. 6. (Color online) ConvLSTM structure incorporating channel space attention mechanism [purple circular X symbol: Hadamard product (element-wise multiplication), $C \times H \times W$: tensor with C channels, each of size $H \times W$].

Table 4
Fault warning hierarchy.

Warning level	Triggering condition	Recommended action
Level I (attention)	Predicted 95th-percentile T > Threshold1 (60 °C) within 1 h	Increase sensor polling rate and notify maintenance for routine check
Level II (warning)	Predicted 50th-percentile T > Threshold1 or 95th-percentile T > Threshold2 (75 °C) within 30 min	Schedule site inspection within 24 h and verify lubrication/loading
Level III (emergency)	Predicted 50th-percentile T > Threshold2 within 15 min	Immediately on-site intervention and prepare for emergency shutdown

4. Results and Discussion

To evaluate performance, the multi-channel (64 channels) sensor data acquisition system with the ConvLSTM model was deployed on a secondary cooling water circulation pump (a rated power of 75 kW). The experiment was conducted for three months, with continuous data acquisition at a frequency of 1 Hz, generating a robust dataset for deep learning training. The dataset encompassed four operational statuses. For normal operation data (80% of total data), baseline data across varying load conditions and ambient temperature fluctuations were collected. For bearing fault data (7.5%), simulated incipient faults were made by reducing lubricant volume, resulting in a gradual 15 °C temperature increase over a 2 h window. For electrical contact fault data (7.5%), a power resistor in the motor junction box was simulated to mimic increased contact resistance, inducing localized thermal anomalies. For transitional status data (5%), start-stop cycles and post-maintenance stabilization were recorded. The data were partitioned into training, validation, and testing sets in a ratio of 70:15:15. The historical observation window was set to 60 min to capture thermal inertia, with a prediction horizon (H-step horizon) of 15 min for early warning.

4.1 ConvLSTM model

In the experiment, sensors were treated as isolated nodes in a cohesive spatiotemporal field. We compared the experimental results using an independent LSTM model and the ConvLSTM model of the developed multichannel sensor data acquisition system, which treated the sensor data array as an 8 × 8 thermal image. The ConvLSTM model significantly reduces prediction error and extends the warning lead time by 150% (Table 5). The results demonstrate the advantages of a coordinated sensor array data processed with ConvLSTM compared with treating sensors as independent streams with standard LSTM. The improvement highlights how spatial correlation enhances predictive accuracy and reliability. The ConvLSTM model reduced the mean absolute error (MAE) from 1.12 to 0.65 °C (42% improvement) and the root mean square error ($RMSE$) from 1.89 to 0.97 °C (49% improvement).

Table 5
Comparison of spatial feature gain analysis between LSTM and ConvLSTM models.

Model	*MAE*	*RMSE*	Average fault warning lead time (min)
LSTM	1.12 °C	1.89 °C	18
ConvLSTM	0.65 °C	0.97 °C	45
Performance improvement	42.0%	48.7%	150%

By modeling the sensor array as a 2D thermal field, the ConvLSTM model leveraged spatial diffusion patterns and filtered out random noise more effectively than independent LSTM streams. The average fault warning lead time increased from 18 to 45 min with a 150% gain. This extended window enables the earlier detection of incipient faults such as bearing friction or motor resistance, giving maintenance teams sufficient time to adjust loads or plan controlled shutdowns rather than resorting to emergency stops. The results showed that dense sensor arrays reduced data volume and enabled spatiotemporal fusion. The ConvLSTM model demonstrated that the advanced deep learning architecture enhanced reliability in harsh industrial environments by validating each sensor's readings against its neighbors.

As shown in Fig. 7, the LSTM model (blue dashed line) exhibited significant lag and underestimation during a bearing overheating event. In contrast, the ConvLSTM model (red line) tracked the measured temperature (black line) with high fidelity, crossing the alarm threshold much earlier. This capability is vital for predictive maintenance, where a minute of lead time might prevent catastrophic mechanical failure.

4.2 ConvLSTM + CBAM model

4.2.1 Predictive accuracy

To quantify the contributions of spatial awareness and attention mechanisms of ConvLSTM and CBAM to sensor-based diagnostics, the effectiveness of the ConvLSTM model was compared with different standard statistical and deep learning models (Table 6). The autoregressive integrated moving average (ARIMA) model showed the highest errors, with an *MAE* of 2.34 °C and an *RMSE* of 3.51 °C. As a linear statistical method, ARIMA was unable to capture the complex, nonlinear thermal transients of high-power pump operations and model long-term dependencies or spatial correlations. LSTM and gated recurrent unit (GRU) models outperformed ARIMA. The GRU model achieved an *MAE* of 0.98 °C, slightly better than that of LSTM at 1.05 °C. These recurrent neural networks are well suited for temporal sequences, allowing them to retain thermal trends over time. However, their performance was limited because they processed the 64-channel array as a flattened one-dimensional vector, losing the spatial context of sensor neighborhoods. The ConvLSTM model delivered a substantial improvement, reducing *MAE* to 0.65 °C and *RMSE* to 0.97 °C. By integrating convolutional

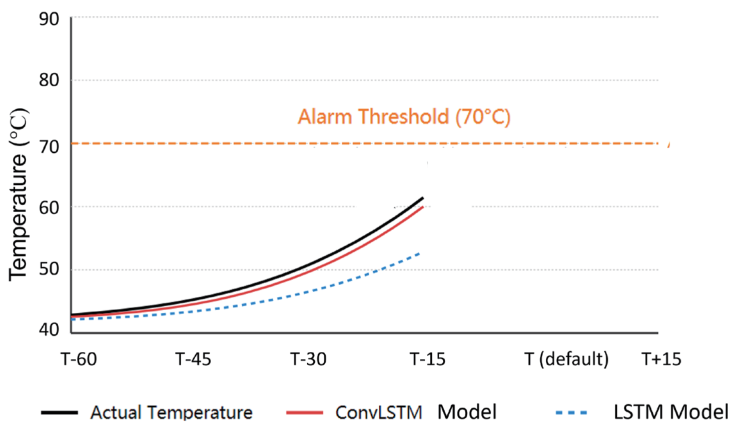

Fig. 7. (Color online) Comparison of predictions of LSTM and ConvLSTM models.

Table 6
Performance comparison of different models.

Model	*MAE* (°C)	*RMSE* (°C)
ARIMA	2.34	3.51
LSTM	1.05	1.76
GRU	0.98	1.65
ConvLSTM	0.65	0.97
ConvLSTM + CBAM	0.50	0.78

layers, the model treated the sensor array as a two-dimensional thermal field, capturing the physical conduction of heat across the pump casing and validating anomalies by cross-referencing neighboring sensors.

The ConvLSTM+CBAM model developed in this study showed the best performance with an *MAE* of 0.50 °C and an *RMSE* of 0.78 °C. The attention mechanism efficiently prioritized critical channels and spatial regions, reducing errors by 23.1% (*MAE*) and 19.6% (*RMSE*) compared with those of the ConvLSTM model. This demonstrates that in a dense sensor array, certain nodes, such as those near bearing housings, carry more information on fault diagnosis, and attention mechanisms effectively deliver high-value data streams.

The results demonstrate that the architecture of the sensor array is essential to enhance the utility of existing hardware. By using a spatiotemporal model with attention, the system developed in this study effectively increases the signal-to-noise ratio of the entire 64-channel array. This proves that intelligent data fusion presents a level of diagnostic precision (sub-degree error) that traditional point-sensing methods cannot match.

4.2.2 Warning lead time

Table 7 shows the operational effectiveness of the system developed in this study by measuring its ability to provide early warning signals across different failure modes. The results highlight shortened warning lead time, which is the most important metric for industrial sensor applications.

The LSTM and GRU models showed average lead times of 18.5 and 21.5 min, respectively. Because these models process sensors as independent one-dimensional time series, they mainly rely on the temporal trend of individual nodes and often trigger alarms only after anomalies have progressed significantly.

The ConvLSTM model extended the lead time to 45 min by treating the 64-channel array as a 2D thermal field. This allowed the system to accurately detect the spatial signature of faults (heat conduction toward neighboring sensors) before a single sensor reached a critical threshold. The ConvLSTM+CBAM model showed the best performance, with an average lead time of 52 min. For bearing faults, the model spent 55 min by focusing on dense sensor clusters near the bearing housing. For motor faults, it spent 49 min by prioritizing regions around the junction box.

To evaluate the diagnostic efficiency of the multi-channel sensor array, we calculated the lead times of the bearing housing and motor casing.[26] These two modules account for more than 80% of unplanned centrifugal pump failures, representing the major M&E degradation vectors. The specific lead time t_{lead} was calculated as

$$t_{lead} = t_{shutdown} - t_{detection}\ , \tag{11}$$

where $t_{shutdown}$ is the physical timestamp when the component's temperature reaches the critical safety shutdown limit (75 °C for bearings, 85 °C for the motor), and $t_{detection}$ is the timestamp at which the model's spatial attention weights and prediction errors statistically deviate beyond a 3σ confidence interval in normal baseline operation. By summing these two values, an aggregate diagnostic metric ($T_{aggregate} = t_{lead,bearing} + t_{lead,motor}$) is calculated to compare overall efficiency across different algorithmic architectures. This combined metric reflects how early the system can recognize diverse thermodynamic fault profiles before they cascade into catastrophic mechanical failures.

Table 7
Average Level I warning lead times of different models.

Model	Bearing fault lead time (min)	Motor fault lead time (min)	Average lead time (min)
LSTM	22	15	18.5
GRU	25	18	21.5
ConvLSTM	48	42	45.0
ConvLSTM + CBAM	55	49	52.0

Compared with standard LSTM, this represents a gain of more than 30 min in detection time. The results show that combining a high-density sensor array with attention-based spatiotemporal modeling extends the diagnostic horizon by nearly threefold compared with that of traditional point-monitoring methods. For a 75 kW pump, the 52 min window transforms fault management from reactive emergency shutdowns to proactive maintenance planning, enabling operators to reduce load or schedule inspections without disrupting cooling water circulation.

The warning lead times of 55 min (for bearing faults) and 49 min (for motor faults) represent baseline averages under progressive, wear-induced thermal degradation. In industrial environments, the actual lead time depends on the physical nature, severity, and propagation velocity of the fault.[25] To evaluate this dependence, we analyzed the model's warning response across two distinct fault scenarios: gradual degradation (surface scratches, lubrication starvation) and sudden structural failures (fatigue fractures, physical cage breakage). The resulting variations in predictive performance are categorized in Table 8.

Progressive surface defects, such as scratches or micro-pitting, produce a slow, highly predictable thermal footprint. This slow thermal diffusion provides the spatiotemporal ConvLSTM structure with historical context to forecast anomalies well in advance, maximizing the lead time up to 65 min. In contrast, a structural fracture or an electrical short circuit triggers a near-instantaneous thermal surge. In catastrophic cases, the lead time is bounded by the time for heat to conduct from the internal point of failure to the external casing where our sensor array is mounted.[25] Such a rapid conduction decreases the warning window to 5–25 min, but the time is sufficient for the automated system to trigger emergency shutdown procedures, successfully preventing severe secondary damage to the pump housing and impellers.

4.2.3 Lead-time sensitivity

Figure 8 shows that the model developed in this study actively extracted spatiotemporal features to identify the physical location of potential failures. At T-10, the spatial attention weights (M_s) are distributed across the 64-sensor array, reflecting the general monitoring of the pump's thermal state. At T-5, as localized heating begins in the motor junction box, the weights

Table 8
Variations in warning lead times and detection margins based on fault progression characteristics.

Fault type	Defect type	Thermal propagation	Average lead time (min)	Alert sensitivity
Gradual (incipient)	Outer race scratch/ micro-pitting	Slow, diffusive heat accumulation	50–65	High (early trend capture)
Gradual (incipient)	Progressive lubrication dryness	Moderately steady thermal climb	40–55	High (early trend capture)
Sudden (catastrophic)	Inner/outer ring fatigue fracture	Rapid friction, thermal shock step	10–25	Moderate (bounded by heat transfer)
Sudden (catastrophic)	Phase-to-phase motor short circuit	Sudden electromagnetic heat spike	5–15	Moderate (bounded by heat transfer)

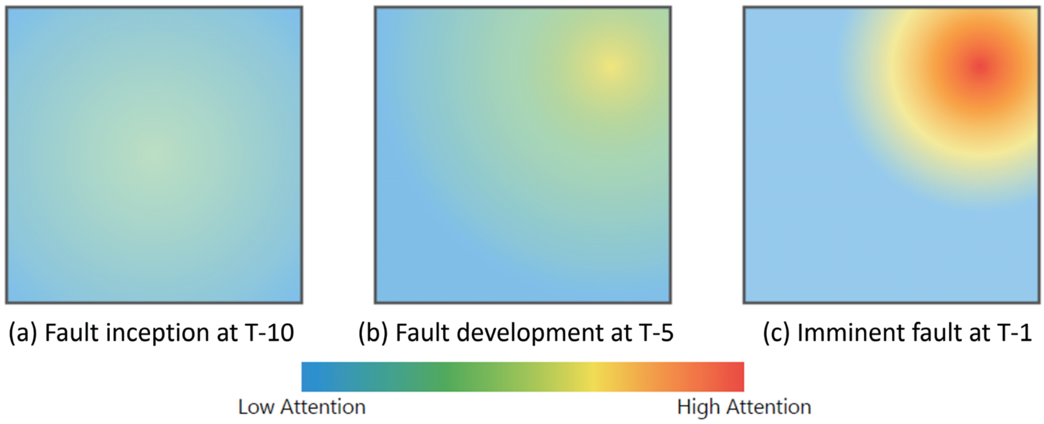

Fig. 8. (Color online) Evolution of spatial attention weights in fault simulation.

cluster in the top-right corner, showing that the model autonomously detects deviations from expected spatial correlations. By T-1, the attention is sharply focused on the hotspot, effectively filtering out irrelevant data to ensure accurate fault prediction. The sharp concentration of attention weights showed that the sensor array offered sufficient spatial resolution to capture localized thermal gradients. This demonstrates that the system functions as a software-defined thermal camera, fusing point-sensor data into a continuous thermal field where the attention mechanism can zoom in on anomalies.

The changes in attention weights extended the lead times (Table 7). By detecting the hotspot at T-5 min, the model issued early warnings with high confidence, reducing the smoothing effect of averaging across the pump and contributing to the low *MAE* of 0.50 °C. Whereas the LSTM model required manual interpretation to produce 64 separate time series data, the ConvLSTM_CBAM model provides an intuitive diagnostic visualization. This helps engineers immediately identify that the fault originates in the motor junction box rather than the bearings.

The developed system predicts faults and pinpoints their positions. This spatial interpretability is obtained from an advanced diagnostic sensor array. In addition to this, the spatial attention weights (M_s) are extracted by the CBAM module during a simulated motor junction box fault. At T−10 min [Fig. 8(a)], during normal baseline operations, the spatial attention weights are distributed evenly across the 64-sensor grid with low relative values (averaging 0.12 ± 0.03), reflecting generalized background monitoring. By T−5 min [Fig. 8(b)], as localized thermal accumulation begins in the motor section, the spatial weights adaptively shift, peaking at 0.68 in the upper-right region. At T−1 min, the critical state [Fig. 8(c)], the spatial attention sharply focuses on the exact physical hotspot coordinates with a peak attention value of 0.94, effectively filtering out ambient thermal background noise.

To complement the spatial attention weights (M_s) and substantiate the interpretability of the channel-wise attention module (M_c), we plotted the normalized channel attention weights across the sensor clusters under different fault states (Fig. 9). Under normal operating conditions, the

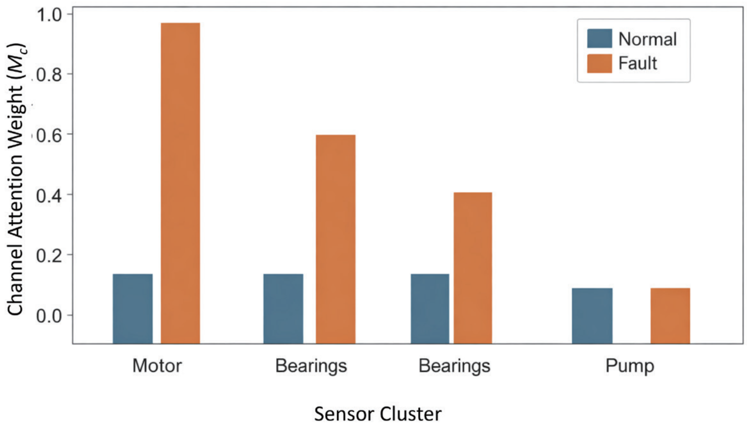

Fig. 9. (Color online) CBAM channel-attention weight (M_c) distribution across sensor clusters during normal states and active thermal anomalies (Bearings in left: a fault attention weight of 0.6, Bearings in right: a fault attention weight of 0.4, Norm: normal state, Fault: abnormal state).

channel attention was distributed uniformly across all monitored zones to secure comprehensive coverage. However, when a bearing lubrication fault was simulated, the attention weights corresponding to the bearing housing channels increased from 0.22 to 0.81, suppressing irrelevant motor fin temperatures. Conversely, during an electrical junction box fault, the motor section channels dominated the channel attention vector (M_c = 0.88). This behavior proves that CBAM successfully learns the underlying physical correlations of heat propagation and dynamically prioritizes high-value sensor nodes without manual thresholding.

4.3 Comparison with Transformer-based spatiotemporal architecture

To validate the positioning and efficiency of the developed ConvLSTM+CBAM model in this study, we compared its performance with two popular attention-driven Transformer variants adapted for spatiotemporal sequence prediction: a Spatiotemporal Vision Transformer (Swin-ST)[26] and the Informer model.[27] Transformers rely on self-attention mechanisms to capture long-range temporal dependencies without the recurrent bottlenecks of LSTM. However, they lack the structural inductive bias of localized spatial convolutions. The quantitative evaluation metrics, including parameter counts, floating point operations (FLOPs), inference latency on an edge-computing module (Raspberry Pi 4B), and prediction accuracy, are shown in Table 9.

The Swin-ST model achieved highly competitive accuracy (*MAE* of 0.52 °C) by utilizing global self-attention across patches of the 2D grid. Its parameter size (24.1 M) and computational complexity (18.5 G FLOPs) are substantially higher than those of our model. This resulted in an inference latency of 162.1 ms, which is a barrier for low-power edge nodes. The Informer model, designed for long-sequence forecasting, suffered from slightly higher errors (*MAE* of 0.58 °C) because flattening the spatial sensor topology into temporal sequence tokens dilutes the localized physical heat-diffusion boundaries across the pump casing.

Table 9
Comparison of performance between the proposed ConvLSTM+CBAM and Transformer variants.

Model	*MAE* (°C)	*RMSE* (°C)	Number of parameters (million)	FLOPs (billion, G)	Inference latency (ms)
Informer(G4)	0.58	0.89	12.4	8.2	84.3
Swin-ST(G3)	0.52	0.79	24.1	18.5	162.1
ConvLSTM + CBAM (this study)	0.5	0.78	3.8	2.1	22.5

In contrast, the ConvLSTM + CBAM model showed the lowest prediction error (*MAE* of 0.50 °C), requiring only 3.8 M parameters and 2.1 G FLOPs. This represents an 84.2% reduction in parameters compared to Swin-ST. By embedding the 2D convolution operation within the recurrent cell, the model preserves spatial priors inherently aligned with the physics of heat conduction. Furthermore, the 22.5 ms latency of our model on edge hardware validates its high suitability and economic feasibility for on-site, real-time industrial deployment on local microcontrollers without relying on expensive cloud computation.

4.4. Real-time edge deployment feasibility

Deep learning architectures containing recurrent and convolutional operations, such as ConvLSTM, can be computationally demanding. To ensure feasibility for resource-constrained industrial edge devices, we investigated two lightweight optimization pathways: structured L1-norm channel pruning and post-training INT8 quantization (PTQ).[28,29] In channel pruning, we pruned 30% of the least significant filters in the spatial convolution layers of the ConvLSTM cell based on their absolute L1-norm weight values, followed by two epochs of fine-tuning to recover accuracy. In INT8 quantization, we converted the network weights and intermediate activations from FP32 to INT8 using TensorFlow Lite's PTQ.

Table 10 shows the performance, latency, and memory footprints of the original and optimized versions of the developed model evaluated on a Raspberry Pi 4B equipped with a 1.5 GHz Broadcom BCM2711 ARM Cortex-A72 CPU. Structured pruning and INT8 quantization reduced the model size by 82.8% (from 15.2 to 2.6 MB) and decreased peak runtime RAM usage from 24.8 to only 4.9 MB. The on-device inference latency per spatiotemporal step decreased from 22.5 to 5.2 ms with an execution speedup of 4.33 times. The cumulative impact on predictive precision was minimal, with MAE rising only marginally from 0.50 to 0.55 °C, which is an acceptable margin for industrial thermal diagnostics. These results showed that the ConvLSTM+CBAM model is highly viable for real-time edge deployment directly alongside the pump hardware.

On the basis of the sensitivity metrics in Table 10, an array of 32 sensors arranged in an 8×4 grid represents the practical minimum needed to match the diagnostic performance of the 64-sensor baseline. In this configuration, prediction error rises modestly from 0.50 to 0.62 °C,

Table 10
Computational overhead and edge latency benchmarks of optimized models.

Model	*MAE* (°C)	Model size (MB)	RAM footprint (MB)	Latency step (ms)	Speed-up factor
FP32 (original)	0.5	15.2	24.8	22.5	1.00×
Pruned FP32	0.51	10.6	18.2	16.1	1.40×
INT8 quantized (PTQ)	0.53	3.8	6.5	8.4	2.68×
Pruned + INT8 Quantized	0.55	2.6	4.9	5.2	4.33×

whereas the system provides a 43 min warning lead time. For industrial deployment, the uniform distribution of 32 sensors is inefficient. Instead, placement should be decided using the spatial attention maps generated by the CBAM module. Concentrating sensors at high-priority coordinates, particularly bearing housings and motor winding interfaces, and spacing them sparsely in low-priority regions, such as outer cooling fans, preserve the sub-degree accuracy of the 64-sensor layout. This targeted installation halves sensor, wiring, and multiplexing hardware requirements, significantly improving economic feasibility for large-scale adoption.

4.5 Economic feasibility

To demonstrate the economic feasibility of deploying a high-density 64-sensor array on a commercial 75 kW water pump system, we performed cost-benefit analysis. Traditional industrial predictive maintenance often relies on periodic high-end handheld IR inspections or vibration analysis systems, which require expensive equipment and expert operators (typically costing USD 10,000 for initial setup and recurring service). In contrast, the hardware component costs of our proposed system are designed for commercial scalability.

$$Total\,Hardware\ \mathrm{Cos}t = N_{sensor} \times \left(C_{PT100} + C_{MAX31865\_node}\right) + C_{MCU} + C_{cabling} \tag{12}$$

Here, C_{PT100} is approximately USD 1.50 per unit and $C_{MAX31865\ node}$ utilizing a multi-channel multiplexed SPI configuration costs approximately USD 2.50 per channel. Including the microcontroller unit (MCU) and industrial shielding cables, the total hardware cost for the 64-channel array is estimated to be less than USD 450. For a standard 75 kW industrial water pump (which typically costs between USD 10,000 and 25,000), this represents an exceptionally low capital investment of less than 2.0 to 4.5%.[30] Since unexpected pump failures and emergency shutdowns in building HVAC or cooling systems can incur losses exceeding USD 8,000 per day in operational downtime and secondary mechanical damage, the system achieves a return on investment within its first prevented failure, making it economically viable for real-world application.

4.6 Limitations and future work

Limitations exist in this study regarding the system's generalizability. Different electromechanical systems, such as air compressors, vacuum pumps, or multi-stage turbines, have distinct thermal boundaries, heat-source locations, and cooling mechanics. The deployment of a model trained on a centrifugal pump onto a different machine class without recalibration might cause performance degradation. To mitigate this, unsupervised domain adaptation and transfer learning must be introduced to the model.[31] By freezing the early spatial feature-extraction convolutional layers of the ConvLSTM cell and fine-tuning only the regression and attention heads using a minimal dataset, for example, 3 to 5 days of baseline operation, new thermal topologies with negligible training overhead can be adopted. Since the developed model in this study utilized a high-density array of 64 sensors in an 8 × 8 grid, the model might operate under lower sensor densities, and a mathematical simulation is required on the testing dataset.

5. Conclusions

An integrated spatiotemporal sensing and prediction system was developed and validated for early thermal fault detection in electromechanical equipment. By deploying a synchronized 64-channel Class A PT100 RTD array, the developed system advanced isolated point monitoring to cohesive thermal field analysis. The ConvLSTM+CBAM mode of the developed system proved effective, achieving a predictive accuracy of 0.50 °C *MAE* and extending the average fault warning lead time to 52 min. The results of the performance evaluation showed that a synchronized array of cost-effective RTDs emulated the diagnostic capabilities of thermal cameras when combined with advanced fusion algorithms. Through the integration of the CBAM's attention mechanism, the sensing layer dynamically prioritizes critical regions, focusing on emerging hotspots without hardware modification. The 150% extension in warning lead time can enable industrial response from reactive emergency responses to proactive maintenance planning. The results of this study show that by combining high-density sensor arrays with spatiotemporal deep learning, the reliability and predictive capability of sensor networks are enhanced in industrial fault monitoring. The developed model provides a foundation for resilient, software-defined equipment monitoring. However, limitations exist, necessitating generalizability enhancement for various machines by validating transfer-learning frameworks across distinct mechanical pump classes and testing self-supervised spatial upsampling methods to maintain sub-degree diagnostic precision even under low sensor density constraints.

Acknowledgments

This research was supported by the Fundamental Research Funds for Beijing Municipal Universities (Project number: 2025F012-JQB).

References

1 M. Lu, H. Liu, and X. Yuan: Trait. Signal **38** (2021) 1095. https://doi.org/10.18280/TS.380420
2 Y. Cheng. IJHT **39** (2021) 1713. https://doi.org/10.18280/IJHT.390603
3 Y. Cheng: IJHT **40** (2021) 604. ttps://doi.org/10.18280/IJHT.400230
4 X. Wang, X. Zhang, F. Zhou, and X. Xu. Mob. Inf. Syst. **2022** (2022) 1710962. https://doi.org/10.1155/2022/1710962
5 W. Sun, H. Gao, Y. Chen, Z. Wang, L. Duan, S. Tan, and X. Fang: Eng. Appl. Artif. Intell. **119** (2023) 105800. https://doi.org/10.1016/J.ENGAPPAI.2022.105800
6 A. Golmohammadi and M. S. Safizadeh: J. Braz. Soc. Mech. Sci. Eng. **45** (2023) 162. https://doi.org/10.1007/S40430-023-04063-7
7 J. Hong, H. Zhang, and X. Xu: Appl. Therm. Eng. **226** (2023) 120304. https://doi.org/10.1016/J.APPLTHERMALENG.2023.120304
8 H. Li, Q. Gao, and Y. Wang: Energies **16** (2023) 5172. https://doi.org/10.3390/EN16135172
9 R. K. Daniels, V. Kumar, S. S. Chouhan, and A. Prabhakar: Appl. Energy **355** (2024) 122352. https://doi.org/10.1016/J.APENERGY.2023.122352
10 Y. N. Agbetossou, K. F. Wotodzo, D. Koffi, L. Nyametso, K. A. Kassegne, and S. Tiem: Curr. J. Appl. Sci. Technol. **43** (2024) 17. https://doi.org/10.9734/CJAST/2024/V43I14340
11 Z. Tang and X. Jian: Sci. Rep. **14** (2024) 5547. https://doi.org/10.1038/S41598-024-56142-X
12 N. Zhang. Int. J. Heat Technol. **42** (2023) 466. https://doi.org/10.18280/IJHT.420212
13 R. K. Daniels, H. Langeh, V. Kumar, S. S. Chouhan, and A. Prabhakar: Appl. Energy **367** (2024) 123299. https://doi.org/10.1016/J.APENERGY.2024.123299
14 N. Said, M. Mansouri, R. Al Hmouz, and A. Khedher: Appl. Sci. **15** (2025) 6263. https://doi.org/10.3390/app15116263
15 R. K. Daniels, V. Kumar, and A. Prabhakar: Renew. Sustain. Energy Rev. **207** (2025) 114925. https://doi.org/10.1016/J.RSER.2024.114925
16 X. Jiang, T. Hu, K. Yao, R. Xiong, J. Qu, Q. Liu, C. Niu, P. Sun, and W. Sima: J. Appl. Polym. Sci. **142** (2024) e56414. https://doi.org/10.1002/APP.56414
17 N. Kardaris, P. Mermigkas, G. Moustris, C. Tzafestas, and P. Maragos: IFAC PapersOnLine **59** (2025) 73. https://doi.org/10.1016/J.IFACOL.2025.08.115
18 S. Wang, L. Zhang, Y. Jia, W. Du, and J. Guo: Ceram. Int. **51** (2025) 20541. https://doi.org/10.1016/J.CERAMINT.2025.02.222
19 C. Lu, J. Lu, and B. Jin: World Electri. Veh. J. **16** (2025) 555. https://doi.org/10.3390/WEVJ16100555
20 T. Bücher, R. Huber, C. Eschenbaum, A. Mertens, U. Lemmer, and H. Amrouch: Sci. Rep. **12** (2022) 14231. https://doi.org/10.1038/s41598-022-18321-6
21 R. Ohara, S. Izumi, S. Imanaka, T. Yamamura, T. Ishii, and H. Kawaguchi: IEEE Access **2** (2024) 124478. https://ieeexplore.ieee.org/stamp/stamp.jsp?arnumber=10643061
22 C. Cao, Y. Tao, L. Yang, Z. Jia, H. Li, Q. Zhong, Z. Xu, and C. Luo: Measurement **259** (2026) 119753. https://doi.org/10.1016/J.MEASUREMENT.2025.119753
23 M. Ge, H. Li, M. Zhang, Z. Li, and S. Leng: J. Physics Conf. Ser. **3174** (2026) 012102. https://doi.org/10.1088/1742-6596/3174/1/012102
24 K. Zhang, J. Qing, H. Jin, and H. Jin: Electronics **14** (2025) 2814. https://doi.org/10.3390/electronics14142814
25 S. Woo, J. Park, J.Y. Lee, and I.S. Kweon: Lect. Notes Comput. Sci. **11211** (2018) 3. https://doi.org/10.1007/978-3-030-01234-2_1
26 H. Mancy and Q. H. Naith: IEEE Access **13** (2025) 48758. https://doi.org/10.1109/ACCESS.2025.3551207
27 G. Zhu, X. Zhang, J. Xu, K. Jiang, J. Yao, Q. Wang, M. Du, Y. Niu, and J. Liu: Eng. Appl. Artif. Intell. **176** (2025) 114774. https://doi.org/10.1016/j.engappai.2026.114774
28 AlZahrani, Y: Discov. Internet Things **6** (2026) 4. https://doi.org/10.1007/s43926-025-00256-9
29 S. Chu and W. Bao: Discov. Comput. **28** (2025) 92. https://doi.org/10.1007/s10791-025-09612-3
30 R. Darko and E.S. Adabor: Comput. Ind. Eng. **217** (2026) 112043. https://doi.org/10.1016/j.cie.2026.112043
31 Y. Liu, A. Deng, G. Chen, Y. Shi, and Q. Hu: Reliab. Eng. Syst. Saf. **257** (2025) 110828. https://doi.org/10.1016/j.ress.2025.110828